Near-field imaging of nonlinear pulse propagation in planar silica waveguides

Y. Linzon,[1] I. Ilsar,[1] D. Cheskis,[1] R. Morandotti,[2] J. S. Aitchison,[3] and S. Bar-Ad[1]

[1]*School of Physics and Astronomy, Raymond and Beverly Sackler Faculty of Exact Sciences, Tel Aviv University, Tel Aviv 69978, Israel*
[2]*Universite' du Quebec, Institute National de la Recherche Scientifique, Varennes, Quebec, Canada J3X 1S2*
[3]*Department of Electrical and Computer Engineering, University of Toronto, Toronto, Ontario, Canada M5S 3G4*

A simplified near-field scanning optical microscope is employed to image the propagation of short laser pulses in planar silica waveguides, in the anomalous dispersion regime, under varying conditions of input beam power and width. Our results show a complex evolution of the transverse intensity profiles of the beam when there is a pronounced difference between the input diffraction and dispersion lengths. Numerical simulations confirm that these complex spatial dynamics are intimately related to the temporal and spectral evolution of the pulse.

Optical solitons are electromagnetic wave packets that propagate inside a material without any change of their shape. They are known to be stable in one-dimensional (1D) systems, where the nonlinear dynamics occur in one transverse dimension only. Realizations include short laser pulses propagating through an optical fiber, where the nonlinear dynamics occur in the time domain, and continuous-wave beams propagating through a slab waveguide, where the nonlinear dynamics occur in one transverse spatial dimension. These examples have been extensively studied in the past [1]. Of greater current interest are multidimensional solitons, with nonlinear dynamics in two or three transverse dimensions, and, in particular, spatiotemporal solitons (STS) that propagate inside the material without diffraction nor dispersion [2]. While symmetrical STS solutions to the nonlinear Schrödinger equation are known to exist when the dispersion is anomalous and the input diffraction and dispersion lengths are equal ($L_{diff}=L_{disp}$), it is also known that in the absence of high-order effects these STS are unstable, and may experience a catastrophic collapse in a finite propagation distance [3]. The fact that in reality this collapse does not occur has stimulated extensive research in the field in an attempt to identify the relevant mechanisms that arrest the collapse, and possibly demonstrate regimes of stability [4,5]. While STS are not accessible in the normal dispersion regime [6], stable propagation in this regime has also been demonstrated [7]. However, the observed wave packets in this case, namely *X* waves, are not fully localized solitary waves, but rather extended (conical) waves that have very localized central peaks.

In experiments involving STS it is desirable to have a full characterization of the beam along the entire length of propagation. This allows better understanding of the dynamics, as well as a direct comparison with numerical simulations. However, it requires that a fraction of the energy of the propagating wave packet be scattered from the waveguide and collected by a suitable apparatus. The scattering is a natural side effect of most waveguide structures, and is often sufficient for imaging the entire evolution of the spatial profile with a simple far-field camera [8]. Such a simple solution, however, is not always possible. In particular, the ex-

tremely low losses in silica glass (the choice material for studies of STS, due to its anomalous dispersion in the near infrared) make such an arrangement impractical, and severely limits our ability to analyze and interpret the results of recent experiments on spatiotemporal dynamics [5,9]. Furthermore, scattering implies an inherent loss mechanism, in the presence of which a true solitary behavior cannot be expected.

In this paper, we introduce an original experimental tool that allows us to follow the spatial dynamics of a beam propagating in planar waveguide structures. We use the concepts of near-field scanning optical microscopy (NSOM) in the collection mode [10]: An optical fiber with a sharp tip is brought within a subwavelength distance from the sample, and collects the evanescent wave, whose power is proportional to that of the coupled beam located directly underneath. Even though the concepts of NSOM are well known [11], and the technique has already been applied in studies of pulse propagation [12], our implementation is unique in its simplicity, and is proven to be sufficient under the current experimental circumstances. It enables us to demonstrate a complex evolution of the transverse intensity profiles of the beam for a narrow input beam ($L_{diff} \ll L_{disp}$). By comparing our experimental data to numerical simulations, we confirm that these spatial dynamics is intimately related to the temporal and spectral evolution of the pulse.

Figure 1 illustrates our experimental setup. We use nearly transform-limited, ≈ 60 fs pulses, at a wavelength of 1520 nm, generated by a Spectra Physics OPA 800 optical parametric amplifier. Inset (a) of Fig. 1 shows the temporal shape of a pulse, measured with a frequency-resolved optical gating (FROG) instrument. A variable neutral-density filter is used to adjust the input power, and a beam splitter (BS) sends a small fraction to the input detector. A ×25 microscope objective is used to shape a ≃ 25 μm wide circular beam with a flat phase front at the input facet of the sample. This narrow-beam excitation (NBE) mode has $L_{diff} \ll L_{disp}$. A cylindrical lens may be inserted in order to shape an elliptical, ≃170 μm wide input beam, for which $L_{diff} \approx L_{disp}$. To this we refer as wide-beam excitation (WBE). In both cases the beam is coupled to a fundamental, transverse magnetic
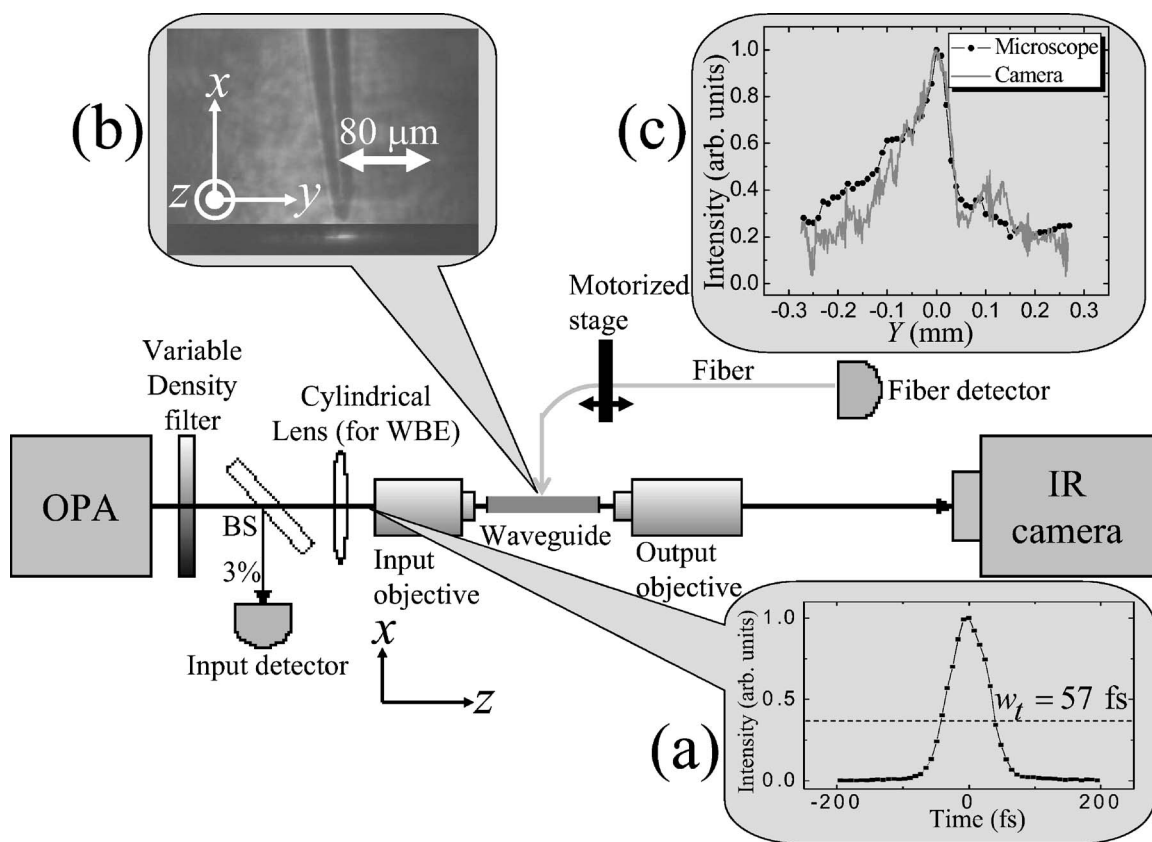
FIG. 1. The experimental setup. Insets: (a) Temporal profile of the input pulse, taken with a Swamp Optics *Grenouille* FROG instrument; (b) overlayed images of the fiber tip and output beam, taken with the far-field IR camera; (c) a comparison of independent measurements, by the microscope and by the camera, of the output beam cross section.

mode of the waveguide in the vertical (X) direction, and begins to diffract in the transverse (Y) direction as it enters the sample and propagates in the Z direction. An output objective images the beam emerging from the output facet onto an infrared camera, for reference.

Our microscope consists of an optical fiber attached to a cantilever arm, one motorized and two mechanical translation stages, and an $In_xGa_{1-x}As$ detector. The fiber has a core diameter of 10 μm and Cr-Al coating. Its cleaved end is coupled to the detector, while the sharpened end is used as the probe. The tip diameter (≈ 4 μm) is large compared to typical NSOM probes, but has sufficient spatial resolution for our purpose, and is less fragile. Inset (b) of Fig. 1 shows a combined image of the fiber tip and a beam emerging from the output facet of the sample. The image was acquired by the far-field infrared camera, which we use to position the tip above the beam path. The fiber is then lowered *manually* until contact is made with the sample. The optical coupling and mechanical friction between the tip and the sample are controlled via the pressure applied by the cantilever arm at the point of contact. They are manually adjusted, according to the signal measured when the tip is sensing the evanescent wave. It is important to note that no change is observed in the far-field camera when the tip comes in contact with the sample. Following tip positioning, the motorized translation stage is used to scan the beam profile along the Y direction. Different Z positions are set manually. The operation of the

microscope is validated by comparing traces of the beam profile at the output facet, obtained independently by the far-field camera and by the scanning tip [inset (c) of Fig. 1].

The sample is a 3 cm long Ge-B-doped silica single-mode waveguide, grown by flame hydrolysis on top of a pure silica clad layer. It has no top clad layer, in order to maximize the amplitude of the evanescent wave. The detected signal is typically 10^{-7} of the signal with the beam itself coupled directly into the fiber, in good agreement with the calculated power in the evanescent wave being $\approx 10^{-3}$ of the power at the center of the waveguide and with the measured coupling efficiency $\approx 10^{-4}$ obtained with the tip oriented parallel to the X direction.

As the dynamics for WBE is considered relatively simple (i.e., diffraction at low intensities, focusing at high intensities, and eventually break-up [5]), we use it as a test case for our microscope. Figure 2 compares the experimental data measured in this configuration to two-dimensional numerical simulations of the NLSE that use the split-step beam propagation method, and take into account stimulated Raman scattering (SRS), self-steepening, and high-order dispersion (HOD) up to fourth order [13]. Figure 2(a) shows spatial cross sections measured with the microscope when the peak power at the input (referring to the power inside the waveguide) is 0.64 MW and the narrowest output beam is observed with the far-field camera. To take into account possible variations of the coupling efficiency to the fiber tip between scans, we have normalized all scans so that the in-
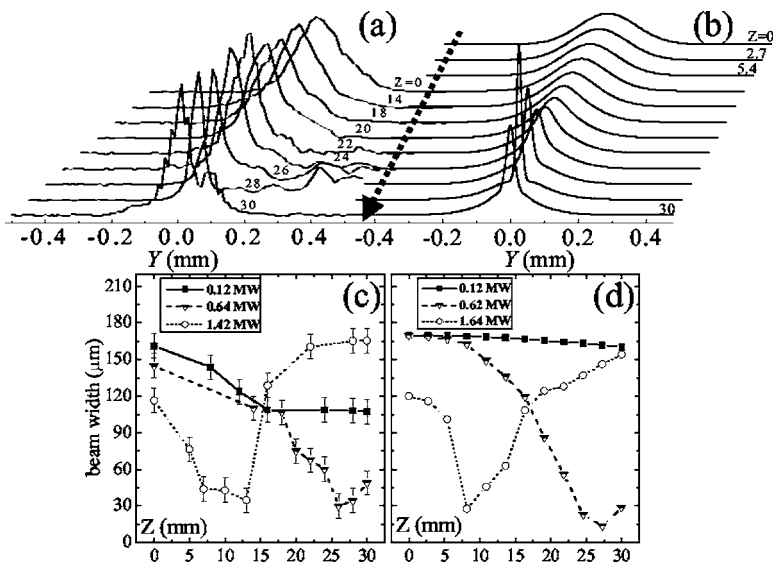
FIG. 2. Results for wide-beam excitation: (a) A set of beam profiles measured at different locations along the Z axis, for an input peak power of 0.64 MW; (b) a set of beam profiles from a simulation for an input peak power of 0.62 MW; (c) and (d) plots of the beam width as a function of Z and the input peak power, for the experimental data and simulations, respectively, extracted from Gaussian fits.

tegrated power is fixed. As expected, the data show a monotonous focusing of the beam, which saturates at a beam width of ≈ 30 μm near the output facet. An identical behavior is obtained in a simulation with the same input conditions, as shown in Fig. 2(b), with a minimum beam width of ≈ 20 μm again reached immediately before the output facet. The good agreement between the experiment and the simulations is emphasized when the beam widths are plotted as a function of Z. Figure 2(c) shows the widths obtained from Gaussian fits to three sets of measurements, at three different input powers, while Fig. 2(d) shows corresponding plots for the simulations. The gradual shift of the beam waist towards the input facet with increasing input power is clearly observed, as is the excellent quantitative agreement between the experimental data and the simulations. This confirms that the dynamics for WBE consist of self-focusing, followed by break-up, with collapse avoided due to HOD. In particular, WBE does not produce solitonlike propagation.

The observed dynamics differs considerably for NBE. At low input powers the beam diffracts strongly, as anticipated due to the short L_{diff} of the input beam. As the power is increased beyond a certain threshold, the beam suddenly focuses and a narrow output is observed in the far-field camera. Our measurements show that in this situation the beam propagates through the sample with only small variations of its spatial extent. This is demonstrated in Fig. 3(a), which shows a set of spatial cross sections for an input peak power of 0.86 MW. Note that the narrow peak at the center is accompanied by satellite peaks that gradually spread away. As the input power is slightly increased to 1.12 MW, the beam image in the far-field camera abruptly expands. The corresponding measurements of the microscope [Fig. 3(b)] indeed show that the narrow peak at the center broadens towards the output facet, and also that the satellite peaks appear earlier and spread away faster. The same behavior is observed in simulations for comparable input parameters, as shown in Figs. 3(c) and 3(d).

In order to understand the nature of the different features observed in the spatial cross sections for NBE, we have measured the spectrum of the light coming out of the sample at

several positions along the Y coordinate. This was done by coupling the fiber tip directly to the output facet (with the fiber oriented parallel to Z), and the cleaved end to a spectrometer. Figure 4 shows that the spectrum at the output facet is position dependent when the input power is high: While the spectrum of the narrow peak at the center [open squares in Fig. 4(b)] is strongly redshifted relative to the input spectrum [Fig. 4(a)], that of the satellite peak 100 μm from the center [full circles in Fig. 4(b)] is only slightly shifted. This
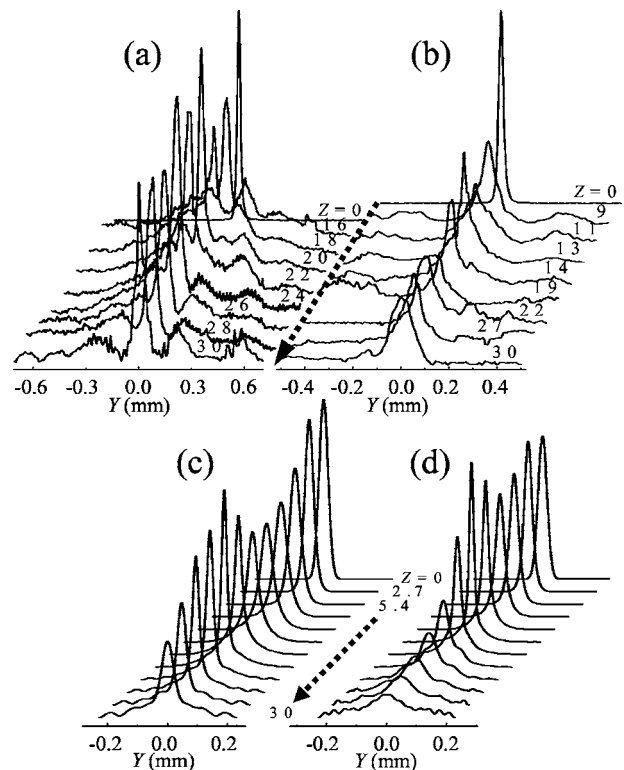

FIG. 3. Results for narrow-beam excitation: (a) and (b) show sets of beam profiles measured at different locations along the Z axis, for input peak powers of 0.86 and 1.12 MW, respectively; (c) and (d) show data for corresponding simulations (0.42 and 0.54 MW, respectively).
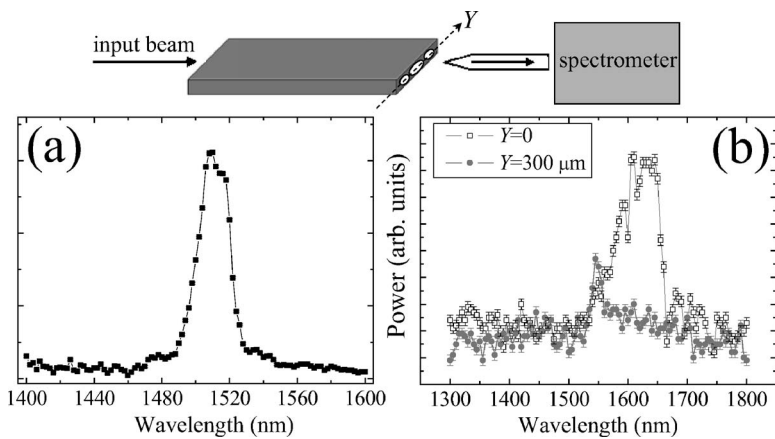
FIG. 4. Spectra measuerd with the fiber microscope for NBE and high input power ($\approx$1 MW peak power): (a) The input spectrum; (b) output spectra on the beam axis (open squares) and $Y=100$ μm off center (full circles).

demonstrates that the different spectral components, which propagate together when the input power is low, become spatially separated as the power is increased beyond the threshold point (we note that the fiber is optimized for the 1300–1550 nm spectral range, and may therefore slightly attenuate the signal at longer wavelengths). This spectral-spatial filtering is also seen in the spectrum of the output beam when the latter is coupled directly to the spectrometer: the $\sim$1500 nm part of that spectrum is strongly suppressed by the placement of an iris at an image plane of the output facet. Further evidence is found in the image of the far-field camera at high input powers, in the form of two distinct planes of focus: we attribute these to the chromatic abberation of the output objective, which dictates a change of focus from the narrow component to the satellite peaks.

A detailed analysis of the simulations confirms the experimental data and explains the origin of the multiple components and their different spectral contents. This can be seen

in Fig. 5, which shows spatiotemporal intensity contour plots of the pulse, for the simulation depicted in Fig. 3(d), and power spectra that were calculated from the corresponding complex amplitudes. The spatiotemporal contour plots at the input (a), at $Z=1.35$ cm (b) and at $Z=2.43$ cm (c) clearly demonstrate the formation of two distinct features as the pulse propagates through the sample. The corresponding spectra are plotted on the right side, with panels (a) and (b) showing the pronounced spectral broadening and self-frequency shift that are due mainly to self-phase modulation and SRS [13]. Two spectra are shown for (c): one was calculated from the temporal cross section on the beam axis ($Y=0$), and corresponds to the narrow spatial feature in Fig. 3(d); the other was calculated from the temporal cross section 88 μm off center, and corresponds to the satellite peaks in Fig. 3(d). In agreement with the experimental data, the latter is centered around the input spectrum, while the former is redshifted. The data in Fig. 5 therefore confirm that a
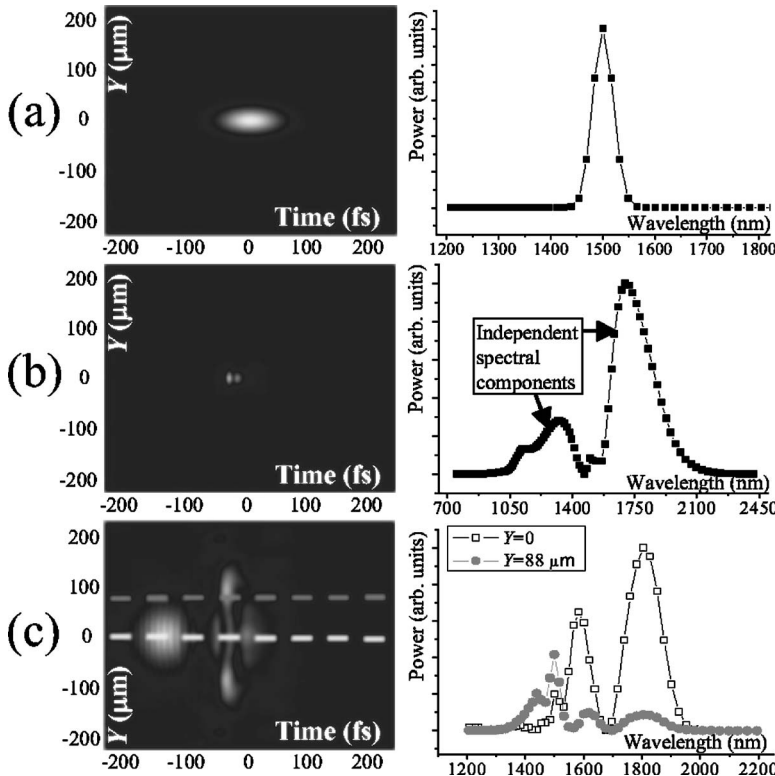

FIG. 5. Spatiotemporal contour plots (left) and power spectra (right) from the numerical simulation of narrow-beam excitation and 0.54 MW input peak power: (a) $Z=0$; (b) $Z=13.5$ mm; (c) $Z=24.3$ mm. The spectra in (a) and (b) are for $Y=0$, while in (c) spectra for $Y=0$ and $Y=88$ μm are presented.

spatial-spectral filtering effect is indeed the origin of the complex dynamics observed in the experiment. More insight is attained by referring to panel (b) of Fig. 5, where the pulse is strongly focused in both space and time, and starts to split in the time domain as a result of HOD [13,14]. Due to SRS, the temporal splitting is accompanied by breakup of the pulse to at least two distinct components with different spectral contents. The combined spectral and temporal separation of these components means that their spatial dynamics also become independent, resulting in strong diffraction of the weak, high-frequency component, and its separation from the strong, self-focusing low-frequency component.

In conclusion, our near-field measurements and computer simulations show a complex evolution of the transverse intensity profiles along the propagation of short laser pulses in planar silica waveguides, in the anomalous dispersion re-

gime, when there is a pronounced difference between the input diffraction and dispersion lengths. We have shown that these complex spatial dynamics are intimately related to the temporal and spectral evolution of the pulse, and take the form of coupled spatial and spectral filtering. While this process inhibits the formation of a true STS in the ideal 2D case, it may clarify several aspects of pulse trapping in lower-dimensionality nonlinear systems such as coupled waveguide arrays [9]. Finally, spectrally resolved characterizations of the evanescent wave are essential for a more detailed understanding of the observed dynamics.

---

[1] J. Opt. Soc. Am. B **14**, 2950 (1997), Special issue; Opt. Quantum Electron. **30**, 501 (1998), special issue.

[2] See, e.g., F. W. Wise and P. Di Trapani, Opt. Photonics News, **13**(2), 28 (2002).

[3] Y. Silberberg, Opt. Lett. **15**, 1282 (1990).

[4] X. Liu, L. J. Qian, and F. W. Wise, Phys. Rev. Lett. **82**, 4631 (1999); X. Liu, K. Beckwitt, and F. Wise, Phys. Rev. E **62**, 1328 (2000).

[5] H. S. Eisenberg, R. Morandotti, Y. Silberberg, S. Bar-Ad, D. Ross, and J. S. Aitchis, Phys. Rev. Lett. **87**, 043902 (2001).

[6] Y.-F. Chen, K. Beckwitt, F. W. Wise, and B. A. Malomed, Phys. Rev. E **70**, 046610 (2004).

[7] P. Di Trapani, G. Valiulis, A. Piskarskas, O. Jedrkiewicz, J. Trull, C. Conti, and S. Trillo, Phys. Rev. Lett. **91**, 093904 (2003).

[8] M. Mitchel, Z. Chen, M.-f Shih, and M. Segev, Phys. Rev.

Lett. **77**, 490 (1996); D. Mandelik, H. Eisenberg, Y. Silberberg, R Morandott, and J. S. Aitchison, *ibid.* **90**, 253902 (2003); A. Fratalocchi, G. Assanto, K. A. Brzdakiewicz, and M. A. Karpierz, Opt. Lett. **29**, 1530 (2004).

[9] D. Cheskis, S. Bar-Ad, R. Morandotti, J. S. Aitchison, H. S. Eisenberg, Y. Silbergerg, and D. Ross, Phys. Rev. Lett. **91**, 223901 (2003).

[10] See, e.g., J. W. P. Hsu, Mater. Sci. Eng., A (R) **33**, 1 (2001).

[11] A. Harootunian, E. Betzig, M. Isaacson, and A. Lewis, Appl. Phys. Lett. **49**, 674 (1986).

[12] M. L. M. Balistreri, H. Gersen, J. P. Korterik, L. Kuipers, and N. F. van Hulst, Science **294**, 1080 (2001).

[13] G. P. Agrawal, *Nonlinear Fiber Optics* (Academic Press, New York, 1995).

[14] C.-C. Chang, H. P. Sardesai, and A. M. Weiner, Opt. Lett. **23**, 283 (1998).